

ARTICLE OPEN



High-performance junction-free field-effect transistor based on blue phosphorene

Shubham Tyagi^{1,2}, Paresh C. Rout^{1,2} and Udo Schwingenschlög¹✉

Two-dimensional semiconductors have great potential in high-performance electronic devices. However, the common way of contacting them with metals to inject charge carriers results in contact resistance. We propose a junction-free field-effect transistor consisting of semiconducting monolayer blue phosphorene as channel material (with high carrier mobility) and metallic bilayer blue phosphorene as electrodes. The junction-free design minimizes the contact resistance. Employing first-principles calculations along with the non-equilibrium Green's function method, we demonstrate a high $I_{\text{on}}/I_{\text{off}}$ ratio of up to 2.6×10^4 and a remarkable transconductance of up to $811 \mu\text{S}/\mu\text{m}$.

npj 2D Materials and Applications (2022)6:86; <https://doi.org/10.1038/s41699-022-00361-1>

INTRODUCTION

Two-dimensional materials currently receive immense attention for application in next-generation electronic devices, particularly as channel materials in field effect transistors (FETs)^{1–5}. Despite an ultrahigh carrier mobility of $\sim 10^5 \text{ cm}^2\text{V}^{-1}\text{s}^{-1}$, graphene cannot be used as channel material due to its zero bandgap nature. Monolayer transition metal dichalcogenides possess (direct) bandgaps of 1–2 eV^{6–9} and provide high $I_{\text{on}}/I_{\text{off}}$ ratios of $\sim 10^5$ – 10^8 ^{10,11}, while low carrier mobilities of $\sim 10^2 \text{ cm}^2\text{V}^{-1}\text{s}^{-1}$ ¹² are not appropriate for high performance applications. Stacking of transition metal dichalcogenides in van der Waals heterostructures can improve the carrier mobility¹³. In addition, such heterostructures provide high $I_{\text{on}}/I_{\text{off}}$ ratios of $\sim 10^3$ for WSe₂–MoS₂ and MoTe₂–SnSe₂¹⁴, $\sim 10^4$ for MoS₂–CuInP₂S₆¹⁵, $\sim 10^6$ for MoTe₂–SnS₂¹⁶, and $\sim 10^7$ for WS₂–graphene¹⁷. However, understanding of the carrier transport and realization of large-area growth are challenges that limit applications^{18,19}. FETs based on wide bandgap oxides such as β -Ga₂O₃ (bandgap of 4.8 eV²⁰; $I_{\text{on}}/I_{\text{off}}$ ratio of $\sim 10^7$ – 10^9 and electron mobility of 32 – $180 \text{ cm}^2\text{V}^{-1}\text{s}^{-1}$ ²¹) and In₂O₃ (bandgap of 3.1 eV²²; $I_{\text{on}}/I_{\text{off}}$ ratio of $\sim 10^6$ and electron mobility of $127 \text{ cm}^2\text{V}^{-1}\text{s}^{-1}$ ²³) provide excellent $I_{\text{on}}/I_{\text{off}}$ ratios but the carrier mobilities are low. Hole mobilities in excess of $10^4 \text{ cm}^2\text{V}^{-1}\text{s}^{-1}$ are predicted for MXenes, a family of two-dimensional transition metal carbides and nitrides^{24,25}. Though they can be employed in FET sensors^{26,27}, application in logic circuits is impeded by degradation in the presence of water and air²⁸. Remarkably, with bandgaps of 0.3–2.0 eV²⁹, monolayer and few-layer black phosphorene achieve competitive hole mobilities of $\sim 10^3 \text{ cm}^2\text{V}^{-1}\text{s}^{-1}$ and $I_{\text{on}}/I_{\text{off}}$ ratios of $\sim 10^5$ ^{30,31} but also degrade in the presence of water and air^{32,33}.

The common metal contacts used to inject charge carriers into the two-dimensional channel material cause Ohmic resistance and/or Schottky barriers that dramatically impact the efficiency of the injection. As it is a great challenge to reduce the contact resistance³⁴, junction-free FETs (consisting of a single material) are an interesting alternative³⁵. While the realization of metallic electrode regions turns out to be difficult, it can be achieved in the case of black and blue phosphorene nanoribbon junction-free FETs by O functionalization³⁶. However, this requires restriction of

the O functionalization to the nanoribbon edges to avoid adverse effects on the material properties^{37,38} and only rather low $I_{\text{on}}/I_{\text{off}}$ ratios of $\sim 10^2$ (with transconductances of $\sim 10^4$) are reported³⁶. In the present work, we demonstrate that these limitations can be overcome by blue phosphorene junction-free FETs. Monolayer blue phosphorene has a bandgap of 1.5–2.0 eV^{32,33} and bilayer blue phosphorene is metallic³⁹. This unique combination of material properties paves the way to junction-free FETs with monolayer blue phosphorene as the semiconducting channel material and bilayer blue phosphorene as the electrode material. We show that such a design gives rise to favorable FET characteristics. The $I_{\text{on}}/I_{\text{off}}$ ratio reaches high values of $\sim 10^4$ due to the junction-free design with low contact resistance. The transconductance is as high as 603 (811) $\mu\text{S}/\mu\text{m}$ for transport along the armchair (zigzag) direction.

RESULTS

Design

Figure 1 shows the optimized structures of monolayer and bilayer blue phosphorene as well as the corresponding band structures and projected densities of states. Monolayer blue phosphorene turns out to be an indirect bandgap semiconductor in agreement with the literature³² and bilayer blue phosphorene turns out to be a metal with an interlayer distance of 1.84 Å in agreement with the literature³⁹. The metallic nature of bilayer blue phosphorene is a result of the short interlayer distance in the energetically favorable A₁B_{–1} stacking. The metallic states are almost equally due to the P 3s, 3p_{x,y} (the p_x and p_y orbitals are degenerate by symmetry), and 3p_z orbitals. The hole mobility of blue phosphorene calculated by deformation potential theory ($2.2 \times 10^3 \text{ cm}^2\text{V}^{-1}\text{s}^{-1}$) clearly exceeds the value reported for black phosphorene ($\sim 10^2 \text{ cm}^2\text{V}^{-1}\text{s}^{-1}$, both experimental and theoretical^{40,41}) and compares well with the value reported for few-layer black phosphorene ($\sim 10^3 \text{ cm}^2\text{V}^{-1}\text{s}^{-1}$ ³⁰).

Figure 2a, e depict the proposed bilayer-monolayer-bilayer FET design with monolayer blue phosphorene serving as the channel material and bilayer blue phosphorene serving as the electrode material. The key advantages are: First, there is no intrinsic strain due to lattice mismatch between the channel and electrode

¹Physical Science and Engineering Division (PSE), King Abdullah University of Science and Technology (KAUST), Thuwal 23955-6900, Saudi Arabia. ²These authors contributed equally: Shubham Tyagi, Paresh C. Rout. ✉email: udo.schwingenschlogl@kaust.edu.sa

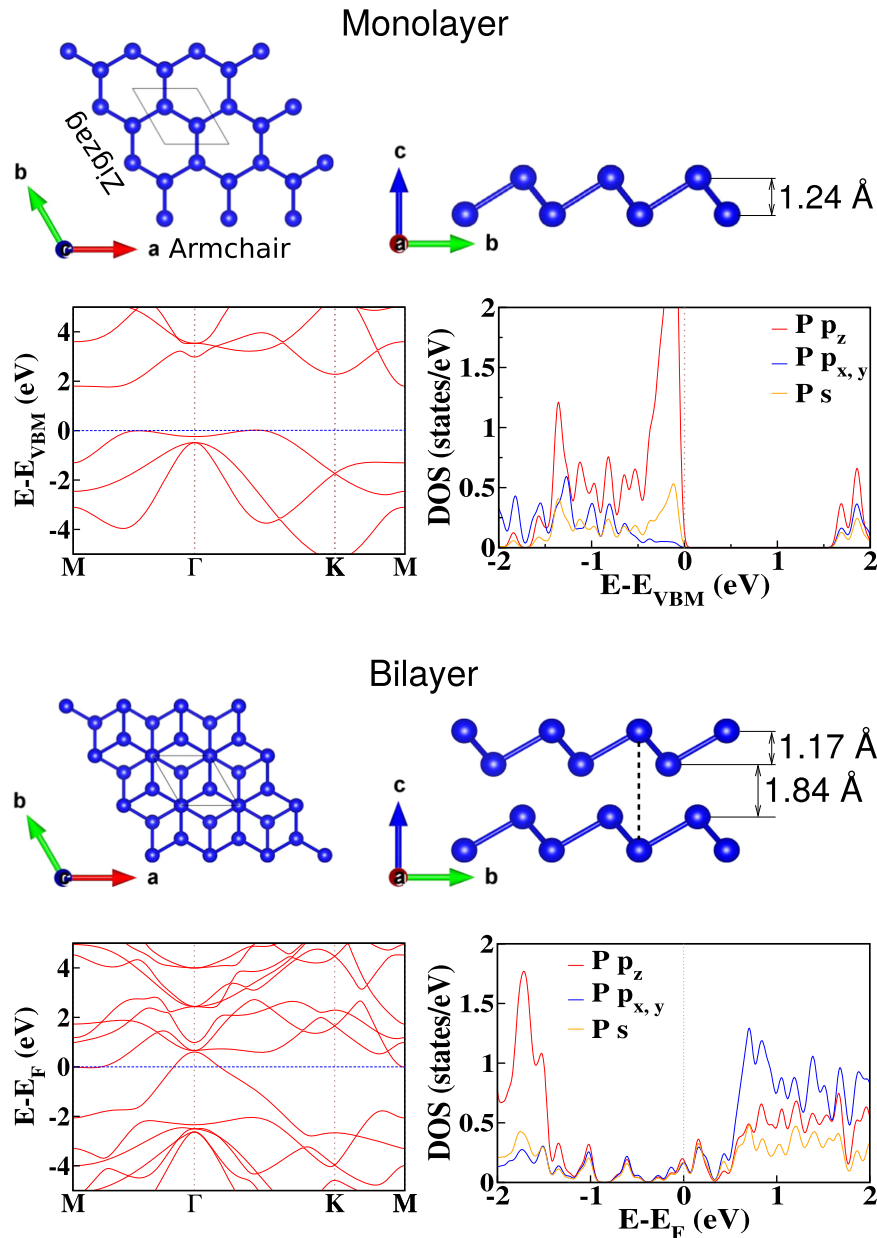


Fig. 1 Monolayer and bilayer blue phosphorene. Top view, side view, band structure (unit cell), and partial densities of states (unit cell) are shown.

materials, since the device is based on blue phosphorene only. Second, the continuous semiconductor-metal contacts reduce the resistance. To quantitatively evaluate the potential of the device, we apply a field-effect gate model⁴², considering transport in both the armchair and zigzag directions.

High quality monolayer blue phosphorene can be grown on Au(111) substrate by molecular beam epitaxy³³, while there is so far no report of synthesis of bilayer blue phosphorene though the material is predicted to be dynamically stable³⁹. It is likely that bilayer blue phosphorene can be fabricated in the energetically favorable A_1B_{-1} stacking by layer transfer techniques, because the large interlayer interaction prevents spontaneous changes in the structure³⁹. Specifically, the wetting transfer method for preparing twisted bilayer graphene⁴³ can be transferred to blue phosphorene due to the fact that the two materials share their hexagonal structure. The method adopts polydimethylsiloxane as substrate for the transfer, which previously was used for transferring monolayer and few-layer black phosphorene^{44–46}. Once bilayer

blue phosphorene is obtained, the proposed bilayer-monolayer-bilayer design can be achieved by local etching. In particular, the atomic layer etching technique enables layer-by-layer etching through alternation between chemical adsorption to modify the exposed layer and physical desorption to remove exactly this modified layer^{47,48}. As an alternative, the methodology of layer-controlled thinning of black phosphorous by an Ar^+ ion beam with narrow energy distribution⁴⁹ can be transferred to blue phosphorene due to the flexible tunability of the Ar^+ ion energy^{50,51}. Chemical vapor deposition opens up another route to the bilayer-monolayer-bilayer design, as it was already used to fabricate monolayer-bilayer-monolayer lateral heterojunctions of transition metal dichalcogenides^{52,53} and to synthesize few-layer black phosphorene from black phosphorous as precursor⁵⁴. The method is transferable to blue phosphorene due to the common hexagonal structure with the transition metal dichalcogenides and the fact that the same precursor can be used as for black phosphorene.

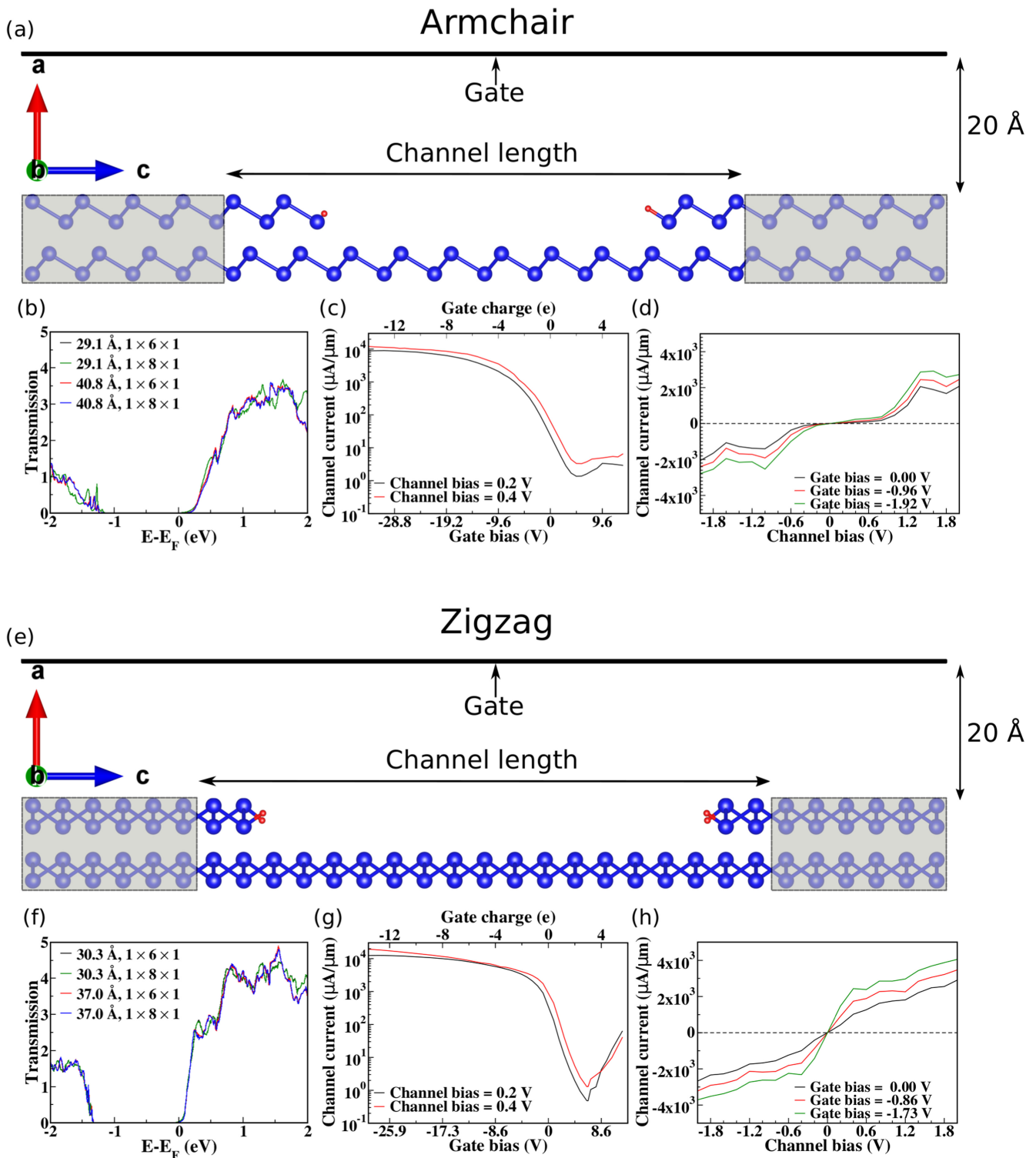


Fig. 2 Armchair and zigzag devices. **a, e** Schematic representations. Blue and red spheres represent the P and H atoms, respectively, and gray color marks the electrodes. **b, f** Transmission spectrum for different channel lengths and k-meshes. **c, g** Channel current as a function of the gate charge for different channel biases. **d, h** I - V characteristics for different gate charges.

Properties

To address the transport, we plot the transmission spectrum obtained for the armchair and zigzag devices in Fig. 2b, f. We find a wide transmission gap that represents the semiconducting channel. As the data show hardly any influence of the channel length, studying a short channel is sufficient to capture the

transport properties of the device in the ballistic regime. It turns out that a $1 \times 6 \times 1$ k-mesh is sufficient to obtain converged results. The first eigenchannel wave function of the left-to-right transmission is plotted in Fig. 3. Due to the symmetry of the FET design, the result for right-to-left transmission (not shown here) is similar with opposite phase⁵⁵. Figure 3 demonstrates delocalization of the first

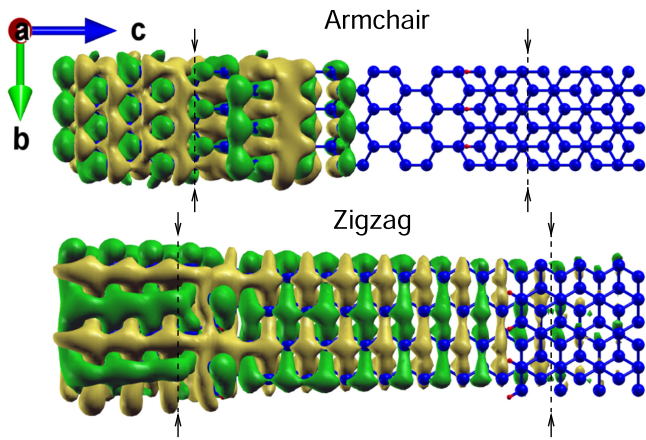


Fig. 3 First transmission eigenchannel wave functions. Results are given for the left-to-right transmission through the armchair and zigzag devices. Green and yellow colors represent the phases. Arrows mark the semiconductor-metal contacts.

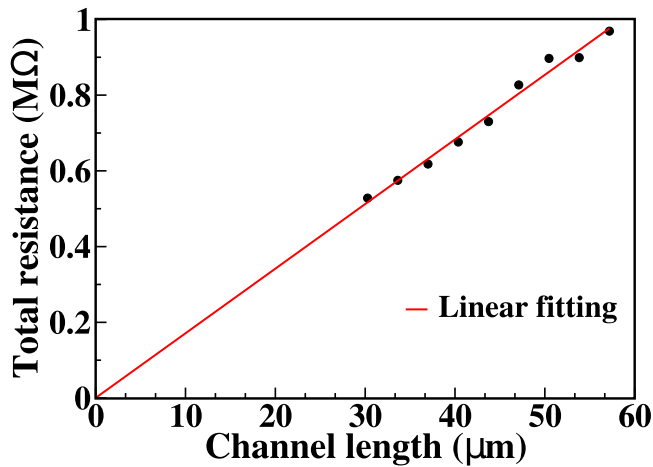


Fig. 4 Total resistance as a function of the channel length. The data refer to the zigzag device.

transmission eigenchannel wave function into the channel region for both the armchair and zigzag directions, and even into the other electrode for the zigzag direction, pointing to excellent coupling at the semiconductor-metal contacts.

Figure 2c, g depicts for the armchair and zigzag devices the channel current as a function of the gate charge at channel biases of 0.2 and 0.4 V. The gate bias is given by the modification of the Hartree potential due to the presence of the gate charge. We obtain I_{on} as the channel current at a gate charge of $13.6 e$ (giving rise to a conservative estimate of the I_{on}/I_{off} ratio) and I_{off} as the minimum of the channel current. At a channel bias of 0.2 V we obtain for transport along the armchair (zigzag) direction $I_{on} = 9.1 \times 10^0$ (1.5×10^1) μA and $I_{off} = 1.3 \times 10^{-3}$ (5.6×10^{-4}) μA , resulting in an I_{on}/I_{off} ratio of 7.0×10^3 (2.6×10^4), while at a channel bias of 0.4 V we obtain $I_{on} = 1.2 \times 10^1$ (2.3×10^1) μA and $I_{off} = 3.3 \times 10^{-3}$ (1.5×10^{-3}) μA , resulting in a lower I_{on}/I_{off} ratio of 4.2×10^3 (1.5×10^4). The obtained I_{on}/I_{off} ratios are significantly higher than those reported for black and blue phosphorene nanoribbon junction-free FETs (2.3×10^2 and 3.5×10^2 , respectively)³⁶ and compare well with the experimental values reported for black phosphorene FETs (10^2 – 10^4)⁵⁶. The threshold voltage estimated by the constant current method for a channel bias of 0.2 V and a channel current of 0.1 μA times the ratio of the gate width and length is -0.4 (1.9) V for the armchair (zigzag) device.

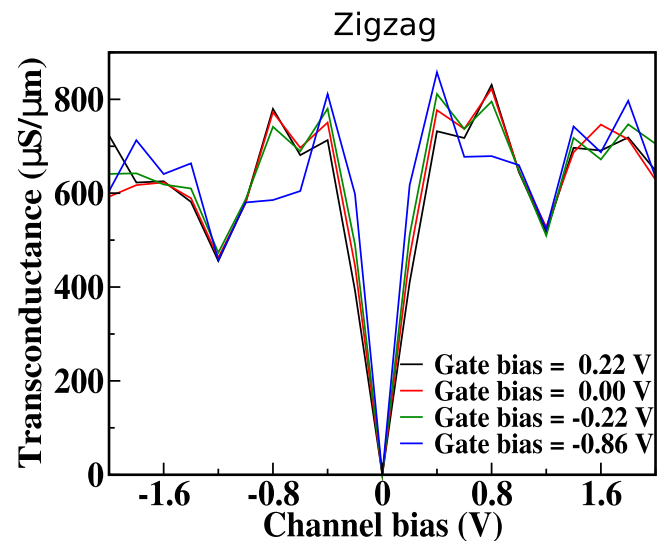
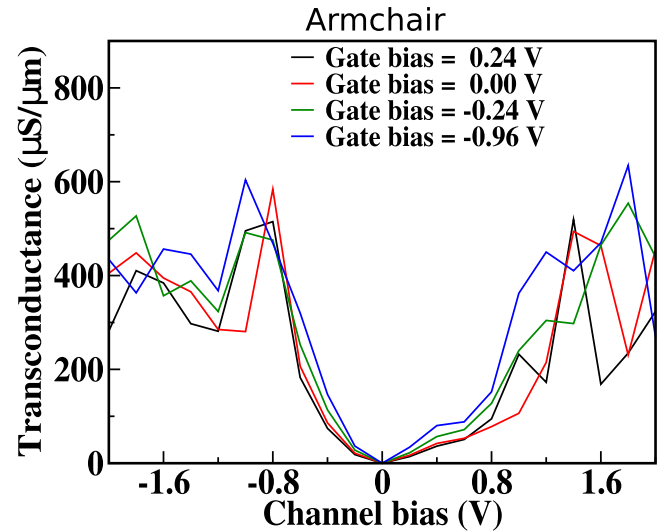


Fig. 5 Transconductances as functions of the channel bias. Results are given for transport along the armchair and zigzag directions.

Figure 2d, h shows for the armchair and zigzag devices that the channel current generally increases with both the channel bias and gate bias. The semiconductor-metal contact of the zigzag device turns out to be Ohmic with efficient charge injection while that of the armchair device is of Schottky type. Using the transfer length method, we obtain from the interception of the linear fitting in Fig. 4 with the total resistance axis for the zigzag device a contact resistance of 3×10^{-4} MΩ. Multiplied with the width of the device this results in $0.3 \Omega \mu m$, which compares very well with experimental reports for graphene ($23 \Omega \mu m$)⁵⁷, Bi-MoS₂ ($123 \Omega \mu m$)⁵⁸, and MoS₂ (200 – $300 \Omega \mu m$)³⁴ devices. The behavior for positive and negative channel bias is very similar for the armchair device, but not precisely the same, since the left and right electrodes are not completely symmetric, see Fig. 2a, e. To quantify the dependence of the channel current on the gate voltage V_{gate} , we calculate the transconductance normalized by the width W of the device (width of the supercell) as $(dI/dV_{gate})/W$ ⁵⁹. We approximate $dI/dV_{gate} = [(I(V_{gate} + \Delta V_{gate}) - I(V_{gate} - \Delta V_{gate}))]/(2\Delta V_{gate})$, where $\Delta V_{gate} = 0.24$ (0.22) V for the armchair (zigzag) device. As expected from the I - V characteristics in Fig. 2d and h, the transconductances in Fig. 5 are higher for the zigzag than the armchair device. At a channel bias of -1.0 V we obtain a transconductance of $603 \mu S/\mu m$ for the armchair device and at a channel bias of -0.4 V we obtain a

transconductance of 811 $\mu\text{S}/\mu\text{m}$ for the zigzag device. These values significantly exceed the experimental values reported for black phosphorene (282 $\mu\text{S}/\mu\text{m}$)⁶⁰ and monolayer MoS_2 (185 $\mu\text{S}/\mu\text{m}$)⁶¹.

DISCUSSION

We propose a junction-free FET based on blue phosphorene, which is semiconducting as a monolayer and metallic as a bilayer. The I - V characteristics obtained for the bilayer-monolayer-bilayer design (does not require doping to create source and drain) demonstrate efficient electron transport between the channel material and electrodes while a decent $I_{\text{on}}/I_{\text{off}}$ ratio is provided. The obtained transconductances outperform competing FETs based on two-dimensional materials. It turns out that a channel length of ~ 30 Å is sufficient to simulate the transport properties of the device. While experimental realization of a device with such a short channel is challenging, an increased channel length will only improve the $I_{\text{on}}/I_{\text{off}}$ ratio of the FET⁶². The transport properties turn out to be slightly better for the zigzag device than the armchair device due to better monolayer-bilayer coupling. From a cost perspective the proposed FET is favorable over junction-free devices based on PdS_2 (requires expensive Pd)³⁵ and phosphorene nanoribbons (requires O functionalization limited to the nanoribbon edges)³⁶. The performance can be further improved by using a gate oxide instead of the simulated vacuum and by optimizing the gate length and underlap (space between the end of the gate and the electrode along the transport direction)⁶³. The proposed FET design can be realized by established fabrication methods.

METHODS

First-principles calculations

We perform first-principles calculations using density functional theory within the generalized gradient approximation of Perdew-Burke-Ernzerhof for the exchange-correlation functional, as implemented in the Quantum-ESPRESSO code⁶⁴. The total energy convergence threshold is set to 10^{-8} Ry and all structures are optimized until the Hellmann-Feynman forces stay below 10^{-5} Ry/bohr. A 80 Ry cut-off is used in the plane wave expansion and a 640 Ry cut-off for the augmentation charge. The first Brillouin zones of monolayer and bilayer blue phosphorene are sampled on Monkhorst-Pack $12 \times 12 \times 1$ k-meshes. The densities of states are calculated by the tetrahedron method with Monkhorst-Pack $24 \times 24 \times 1$ k-meshes. Periodic boundary conditions are used with 20 Å vacuum slabs to create two-dimensional models.

Transport calculations

Transport calculations are performed adopting the non-equilibrium Green's function method in combination with density functional theory⁶⁵, which provides excellent agreement with experimental results^{63,66}. A 300 Ry cut-off is used for the double-zeta polarized basis set. Monkhorst-Pack $1 \times 6 \times 100$ k-meshes are employed for the semi-infinite electrode calculations and Monkhorst-Pack $1 \times 6 \times 1$ k-meshes for the transport calculations. The transmission spectrum of electrons with energy E subject to a channel bias V between the electrodes (bilayer blue phosphorene) through the scattering region (monolayer blue phosphorene) is calculated as⁶⁷

$$T(E, V) = \text{Tr}[-G(E, V)[\Sigma_L(E) - \Sigma_L^\dagger(E, V)]G^\dagger(E, V)[\Sigma_R(E) - \Sigma_R^\dagger(E, V)]], \quad (1)$$

where $G(E, V)$ is the retarded Green's function of the scattering region and $\Sigma_{L,R}(E, V)$ are the self-energies of the left (L) and right (R) electrodes. The current is given by⁶⁷

$$I(V) = \frac{2e}{h} \int_{-\infty}^{\infty} [f(E - (E_F - eV/2)) - f(E - (E_F + eV/2))] T(E, V) dE, \quad (2)$$

where f is the Fermi-Dirac distribution function, E_F is the Fermi energy, and e is the elementary charge. We consider a $1 \times 3 \times 5$ ($1 \times 2 \times 9$) supercell of monolayer blue phosphorene to model the channel material and a $1 \times 3 \times 2$ ($1 \times 2 \times 3$) supercell of bilayer blue phosphorene to model the electrodes for transport along the armchair (zigzag) direction. The in-plane supercell dimensions given as width \times length are 10.09×29.13 (11.65×30.27) Å² for the channel material and 10.09×11.65 (11.65×10.09) Å² for the electrodes. A uniformly charged gate is added at a distance of 20 Å in the out-of-plane direction to realize a FET geometry. The transmission eigenchannel wave functions are calculated by means of the inelastica package⁶⁸.

DATA AVAILABILITY

The datasets generated and analyzed during the current study are available from the corresponding author on reasonable request.

Received: 27 January 2022; Accepted: 3 November 2022;

Published online: 09 December 2022

REFERENCES

- Schwierz, F., Pezoldt, J. & Granzner, R. Two-dimensional materials and their prospects in transistor electronics. *Nanoscale* **7**, 8261–8283 (2015).
- Chhowalla, M., Jena, D. & Zhang, H. Two-dimensional semiconductors for transistors. *Nat. Rev. Mater.* **1**, 16052 (2016).
- Eftekhari, A. Tungsten dichalcogenides (WS_2 , WSe_2 , and WTe_2): materials chemistry and applications. *J. Mater. Chem. A* **5**, 18299–18325 (2017).
- Zeng, M., Xiao, Y., Liu, J., Yang, K. & Fu, L. Exploring two-dimensional materials toward the next-generation circuits: from monomer design to assembly control. *Chem. Rev.* **118**, 6236–6296 (2018).
- Qian, Q. et al. 2D materials as semiconducting gate for field-effect transistors with inherent over-voltage protection and boosted ON-current. *NPJ 2D Mater. Appl.* **3**, 24–32 (2019).
- Kuc, A., Zibouche, N. & Heine, T. Influence of quantum confinement on the electronic structure of the transition metal sulfide TS_2 . *Phys. Rev. B* **83**, 245213 (2011).
- Yun, W. S., Han, S. W., Hong, S. C., Kim, I. G. & Lee, J. D. Thickness and strain effects on electronic structures of transition metal dichalcogenides: 2H-MX₂ semiconductors (M = Mo, W; X = S, Se, Te). *Phys. Rev. B* **85**, 033305 (2012).
- Tongay, S. et al. Thermally driven crossover from indirect toward direct bandgap in 2D semiconductors: MoSe_2 versus MoS_2 . *Nano Lett.* **12**, 5576–5580 (2012).
- Yazyev, O. V. & Kis, A. MoS_2 and semiconductors in the flatland. *Mater. Today* **18**, 20–30 (2015).
- Radisavljevic, B., Radenovic, A., Brivio, J., Giacometti, V. & Kis, A. Single-layer MoS_2 transistors. *Nat. Nanotechnol.* **6**, 147–150 (2011).
- Hwang, W. S. et al. Transistors with chemically synthesized layered semiconductor WS_2 exhibiting 10^5 room temperature modulation and ambipolar behavior. *Appl. Phys. Lett.* **101**, 013107 (2012).
- Yu, Z. et al. Analyzing the carrier mobility in transition-metal dichalcogenide MoS_2 field-effect transistors. *Adv. Funct. Mater.* **27**, 1604093 (2017).
- Xu, L. et al. Enhanced electrical performance of van der Waals heterostructure. *Adv. Mater. Interfaces* **8**, 2001850 (2021).
- Li, C. et al. $\text{WSe}_2/\text{MoS}_2$ and $\text{MoTe}_2/\text{SnSe}_2$ van der Waals heterostructure transistors with different band alignment. *Nanotechnol.* **28**, 415201 (2017).
- Si, M., Liao, P.-Y., Qiu, G., Duan, Y. & Ye, P. D. Ferroelectric field-effect transistors based on MoS_2 and CuInP_2S_6 two-dimensional van der Waals heterostructure. *ACS Nano* **12**, 6700–6705 (2018).
- Szabo, A., Koester, S. J. & Luisier, M. Ab-initio simulation of van der Waals MoTe_2 - SnS_2 heterotunneling FETs for low-power electronics. *IEEE Electron Device Lett.* **36**, 514–516 (2015).
- Yeh, C.-H., Cao, W., Pal, A., Parto, K. & Banerjee, K. Area-selective-CVD technology enabled top-gated and scalable 2D-heterojunction transistors with dynamically tunable Schottky barrier. In *IEEE International Electron Devices Meeting* 23.4.1–23.4.4 (2019).
- Liu, Y., Huang, Y. & Duan, X. Van der Waals integration before and beyond two-dimensional materials. *Nature* **567**, 323–333 (2019).
- Liang, S.-J., Cheng, B., Cui, X. & Miao, F. Van der Waals heterostructures for high-performance device applications: challenges and opportunities. *Adv. Mater.* **32**, 1903800 (2020).

20. Xue, H. et al. An overview of the ultrawide bandgap Ga₂O₃ semiconductor-based Schottky barrier diode for power electronics application. *Nanoscale Res. Lett.* **13**, 290 (2018).
21. Chabak, K. D. et al. Lateral β -Ga₂O₃ field effect transistors. *Semicond. Sci. Technol.* **35**, 013002 (2019).
22. Li, Q. et al. Gas-mediated liquid metal printing toward large-scale 2D semiconductors and ultraviolet photodetector. *NPJ 2D Mater. Appl.* **5**, 36–45 (2021).
23. Nayak, P. K., Hedhili, M. N., Cha, D. & Alshareef, H. N. High performance In₂O₃ thin film transistors using chemically derived aluminum oxide dielectric. *Appl. Phys. Lett.* **103**, 033518 (2013).
24. Zhang, X., Zhao, X., Wu, D., Jing, Y. & Zhou, Z. High and anisotropic carrier mobility in experimentally possible Ti₂CO₂ (MXene) monolayers and nanoribbons. *Nanoscale* **7**, 16020–16025 (2015).
25. Zha, X.-H. et al. The thermal and electrical properties of the promising semiconductor MXene Hf₂CO₂. *Sci. Rep.* **6**, 27971 (2016).
26. Xu, B. et al. Ultrathin MXene-micropattern-based field-effect transistor for probing neural activity. *Adv. Mater.* **28**, 3333–3339 (2016).
27. Li, Y. et al. MXene-graphene field-effect transistor sensing of influenza virus and SARS-CoV-2. *ACS Omega* **6**, 6643–6653 (2021).
28. Mashtalir, O. et al. Dye adsorption and decomposition on two-dimensional titanium carbide in aqueous media. *J. Mater. Chem. A* **2**, 14334–14338 (2014).
29. Qiao, J., Kong, X., Hu, Z.-X., Yang, F. & Ji, W. High-mobility transport anisotropy and linear dichroism in few-layer black phosphorus. *Nat. Commun.* **5**, 4475 (2014).
30. Li, L. et al. Black phosphorus field-effect transistors. *Nat. Nanotechnol.* **9**, 372–377 (2014).
31. Ling, X., Wang, H., Huang, S., Xia, F. & Dresselhaus, M. S. The renaissance of black phosphorus. *Proc. Natl. Acad. Sci. USA* **112**, 4523–4530 (2015).
32. Zhu, Z. & Tománek, D. Semiconducting layered blue phosphorus: a computational study. *Phys. Rev. Lett.* **112**, 176802 (2014).
33. Zhang, J. L. et al. Epitaxial growth of single layer blue phosphorus: a new phase of two-dimensional phosphorus. *Nano Lett.* **16**, 4903–4908 (2016).
34. Kappera, R. et al. Phase-engineered low-resistance contacts for ultrathin MoS₂ transistors. *Nat. Mater.* **13**, 1128–1134 (2014).
35. Ghorbani-Asl, M., Kuc, A., Miro, P. & Heine, T. A single-material logical junction based on 2D crystal PdS₂. *Adv. Mater.* **28**, 853–856 (2016).
36. Montes, E. & Schwingschlögl, U. High-performance field-effect transistors based on α P and β P. *Adv. Mater.* **31**, 1807810 (2019).
37. Huang, Y. et al. Interaction of black phosphorus with oxygen and water. *Chem. Mater.* **28**, 8330–8339 (2016).
38. Mir, S. H., Yadav, V. K. & Singh, J. K. Recent advances in the carrier mobility of two-dimensional materials: a theoretical perspective. *ACS Omega* **5**, 14203–14211 (2020).
39. Arcudia, J., Kempt, R., Cifuentes-Quintal, M. E., Heine, T. & Merino, G. Blue phosphorene bilayer is a two-dimensional metal and an unambiguous classification scheme for buckled hexagonal bilayers. *Phys. Rev. Lett.* **125**, 196401 (2020).
40. Liu, H. et al. Phosphorene: an unexplored 2D semiconductor with a high hole mobility. *ACS Nano* **8**, 4033–4041 (2014).
41. Xiao, J. et al. Theoretical predictions on the electronic structure and charge carrier mobility in 2D phosphorus sheets. *Sci. Rep.* **5**, 9961 (2015).
42. Papior, N., Gunst, T., Stradi, D. & Brandbyge, M. Manipulating the voltage drop in graphene nanojunctions using a gate potential. *Phys. Chem. Chem. Phys.* **18**, 1025–1031 (2016).
43. Hou, Y. et al. Preparation of twisted bilayer graphene via the wetting transfer method. *ACS Appl. Mater. Interfaces* **12**, 40958–40967 (2020).
44. Island, J. O., Steele, G. A., van der Zant, H. S. J. & Castellanos-Gomez, A. Environmental instability of few-layer black phosphorus. *2D Mater.* **2**, 011002 (2015).
45. Favron, A. et al. Photooxidation and quantum confinement effects in exfoliated black phosphorus. *Nat. Mater.* **14**, 826–832 (2015).
46. Lee, Y. et al. Fabrication and imaging of monolayer phosphorene with preferred edge configurations via graphene-assisted layer-by-layer thinning. *Nano Lett.* **20**, 559–566 (2019).
47. Kanarik, K. J. et al. Overview of atomic layer etching in the semiconductor industry. *J. Vac. Sci. Technol.* **33**, 020802 (2015).
48. Kim, K. S. et al. Atomic layer etching of graphene through controlled ion beam for graphene-based electronics. *Sci. Rep.* **7**, 2462 (2017).
49. Park, J. W. et al. Layer-controlled thinning of black phosphorus by an Ar ion beam. *J. Mater. Chem. C* **5**, 10888–10893 (2017).
50. Kabiraj, D. & Ghosh, S. Defect engineering in GaAs using high energy light ion irradiation: role of electronic energy loss. *J. Appl. Phys.* **109**, 033701 (2011).
51. Li, Z. & Chen, F. Ion beam modification of two-dimensional materials: characterization, properties, and applications. *Appl. Phys. Rev.* **4**, 011103 (2017).
52. Zhang, C. et al. Visualizing band offsets and edge states in bilayer-monolayer transition metal dichalcogenides lateral heterojunction. *Nat. Commun.* **7**, 10349 (2016).
53. Mandyam, S. V. et al. Controlled growth of large-area bilayer tungsten diselenides with lateral p-n junctions. *ACS Nano* **13**, 10490–10498 (2019).
54. Smith, J. B., Hagaman, D. & Ji, H.-F. Growth of 2D black phosphorus film from chemical vapor deposition. *Nanotechnol.* **27**, 215602 (2016).
55. Paulsson, M. & Brandbyge, M. Transmission eigenchannels from nonequilibrium Green's functions. *Phys. Rev. B* **76**, 115117 (2007).
56. Illarionov, Y. Y. et al. Highly-stable black phosphorus field-effect transistors with low density of oxide traps. *NPJ 2D Mater. Appl.* **1**, 23–29 (2017).
57. Anzi, L. et al. Ultra-low contact resistance in graphene devices at the Dirac point. *2D Mater.* **5**, 025014 (2018).
58. Shen, P.-C. et al. Ultralow contact resistance between semimetal and monolayer semiconductors. *Nature* **593**, 211–217 (2021).
59. Javey, A. et al. High- κ dielectrics for advanced carbon-nanotube transistors and logic gates. *Nat. Mater.* **1**, 241–246 (2002).
60. Haratipour, N. & Koester, S. J. Ambipolar black phosphorus MOSFETs with record n-channel transconductance. *IEEE Electron Device Lett.* **37**, 103–106 (2016).
61. Arutchelvan, G. et al. Impact of device scaling on the electrical properties of MoS₂ field-effect transistors. *Sci. Rep.* **11**, 6610 (2021).
62. Liu, H., Neal, A. T. & Ye, P. D. Channel length scaling of MoS₂ MOSFETs. *ACS Nano* **6**, 8563–8569 (2012).
63. Quhe, R. et al. Simulations of quantum transport in sub-5-nm monolayer phosphorene transistors. *Phys. Rev. Appl.* **10**, 024022 (2018).
64. Giannozzi, P. et al. QUANTUM ESPRESSO: a modular and open-source software project for quantum simulations of materials. *J. Phys. Condens. Mater.* **21**, 395502 (2006).
65. Brandbyge, M., Mozos, J. L., Ordejón, P., Taylor, J. & Stokbro, K. Density-functional method for nonequilibrium electron transport. *Phys. Rev. B* **65**, 165401 (2002).
66. Desai, S. B. et al. MoS₂ transistors with 1-nanometer gate lengths. *Science* **354**, 99–102 (2016).
67. Datta, S. *Quantum transport: Atom to transistor* (Cambridge University Press, 2005).
68. Frederiksen, T., Paulsson, M., Brandbyge, M. & Jauho, A.-P. Inelastic transport theory from first principles: methodology and application to nanoscale devices. *Phys. Rev. B* **75**, 205413 (2007).

ACKNOWLEDGEMENTS

The research reported in this publication was supported by funding from King Abdullah University of Science and Technology (KAUST). For computer time, this research used the resources of the Supercomputing Laboratory at KAUST.

AUTHOR CONTRIBUTIONS

S.T. executed the calculations. P.C.R. and U.S. contributed to the interpretation of the data and writing of the manuscript.

COMPETING INTERESTS

The authors declare no competing interests.

ADDITIONAL INFORMATION

Correspondence and requests for materials should be addressed to Udo Schwingschlögl.

Reprints and permission information is available at <http://www.nature.com/reprints>

Publisher's note Springer Nature remains neutral with regard to jurisdictional claims in published maps and institutional affiliations.



Open Access This article is licensed under a Creative Commons Attribution 4.0 International License, which permits use, sharing, adaptation, distribution and reproduction in any medium or format, as long as you give appropriate credit to the original author(s) and the source, provide a link to the Creative Commons license, and indicate if changes were made. The images or other third party material in this article are included in the article's Creative Commons license, unless indicated otherwise in a credit line to the material. If material is not included in the article's Creative Commons license and your intended use is not permitted by statutory regulation or exceeds the permitted use, you will need to obtain permission directly from the copyright holder. To view a copy of this license, visit <http://creativecommons.org/licenses/by/4.0/>.